Experimental Data for JBC Resistance, Sinkage, Trim, Self-Propulsion Factors, Longitudinal Wave Cut and Detailed Flow with and without an Energy Saving Circular Duct

Nobuyuki Hirata, Hiroshi Kobayashi, Takanori Hino, Yasuyuki Toda, Moustafa Abdel-Maksoud, and Frederick Stern

Abstract In this Chapter, measured data of resistance, sinkage, trim, self-propulsion factors, longitudinal wave cut and detailed flow are summarized for Japan Bulk Carrier (JBC) with and without an energy saving circular duct. JBC is a newly designed ship for CFD validation of a ship with an energy saving device (ESD). Resistance and self-propulsion tests are conducted in towing tanks of National Maritime Research Institute (NMRI) and Osaka University (OU) using model ships of different sizes. Detailed local flow data are acquired using SPIV (Stereo Particle Image Velocimetry) for several cross sections at towing tanks of NMRI and OU. The local flow data are also measured by SPIV in a wind tunnel at Hamburg University of Technology (TUHH).

1 Introduction

New test cases associated with hydrodynamics of flows around a ship equipped with an energy saving device (ESD) are adopted in T2015 Workshop. A ship hull called Japan Bulk Carrier (JBC) which is a Cape-size bulk carrier was designed together with a circular duct in front of a propeller as an ESD.

N. Hirata · H. Kobayashi
National Maritime Research Institute, Mitaka, Japan

T. Hino (✉)
Yokohama National University, Yokohama, Japan
e-mail: hino-takanori-nf@ynu.ac.jp

Y. Toda
Osaka University, Suita, Japan

M. Abdel-Maksoud
Hamburg University of Technology, Hamburg, Germany

F. Stern
University of Iowa and Iowa Institute of Hydraulic Research (IIHR), Iowa, IA, USA

Validation data for the test cases were obtained by model tests in the multiple facilities including National Maritime Research Institute (NMRI), Osaka University (OU) and Hamburg University of Technology (TUHH). Resistance and self-propulsion tests were conducted at the towing tanks of NMRI and OU. In addition, local flow measurements are carried out at two towing tanks on NMRI and OU, and also at the wind tunnel of TUHH.

In this chapter, description of the ship hull, the propeller and the energy saving duct is given first. It is followed by the summary of towing tank tests. The next section is devoted to the local velocity measurements. Accuracy estimations are given for NMRI measurement and credibility of SPIV (Stereo Particle Image Velocimetry) data of three facilities is discussed. The next section gives the wave height measurement results at NMRI towing tank. Conclusions of the chapter are summarised in the last section.

2 JBC (Japan Bulk Carrier)

2.1 Ship Hull

Japan Bulk Carrier (JBC) is a Cape-size bulk carrier designed for the validation of CFD analysis of a ship with an energy saving device (ESD). A ship type of a bulk carrier is selected since it is one of the major cargo vessels in international shipping and since a blunt ship hull is considered to be appropriate for the examination of an effect of ESDs. A circular duct placed ahead of a propeller is adopted as an ESD. The ship hull and the duct have been newly designed in the collaborative research project in Japan which were organized by universities, research organizations and shipyards in Japan under the sponsorship of ClassNK (Hino et al. 2016).

The principal particulars of a ship are determined following the representative values of current vessels as shown in Table 1. The design speed is set to 14.5 knots which corresponds to $F_n(L_{PP}) = U_0/\sqrt{gL_{PP}} = 0.142$. Based on the comparative study (Hino et al. 2016) of resistance and wake distributions at a propeller plane by numerical simulations at the design Froude number $F_n = 0.142$ and the model scale Reynolds number $R_n(L_{PP}) = 7.245 \times 10^6$, the final hull form is designed as shown in Fig. 1.
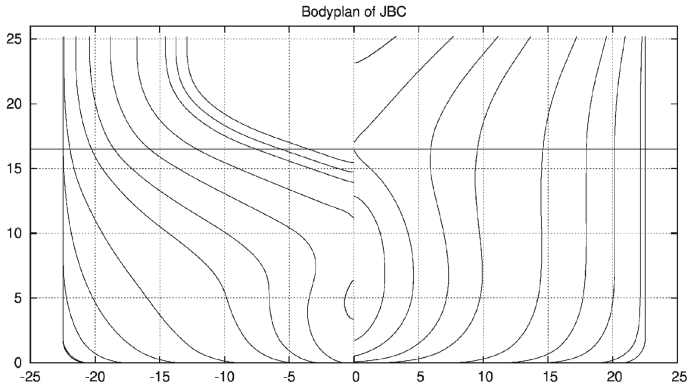
2.2 Propeller

A propeller used is a conventional five-bladed MAU type propeller. The particulars of the model propeller for a model ship of $L_{PP} = 7.000$ m are shown in Table 2.

Table 1 Principal particulars of JBC in actual ship scale

Length between perpendiculars	L_{PP} (m)	280.0
Length of waterline	L_{WL} (m)	285.0
Maximum beam of waterline	B_{WL} (m)	45.0
Depth	D (m)	25.0
Draft	T (m)	16.5
Displacement volume	∇ (m3)	178369.9
Wetted surface area w/o ESD	$S_{\text{w/oESD}}$ (m2)	19556.1
Wetted surface area with ESD	S_{withESD} (m2)	19633.9
Block coefficient (C_B)	$\nabla/(L_{PP}B_{WL}T)$	0.8580
Midship section coefficient (C_M)		0.9981
LCB (%L_{PP}), fwd+		2.5475
Vertical Center of Gravity (from keel)*1	KG (m)	13.29
Metacentric height*1	GM (m)	5.3
Moment of Inertia*1	K_{xx}/B_{WL}	0.40
Moment of Inertia*1	K_{yy}/B_{WL}, K_{zz}/B_{WL}	0.25
Propeller center, longitudinal location (from FP)	x/L_{PP}	0.9864
Propeller center, vertical location (below waterline)	$-z/L_{PP}$	0.0404214
Propeller rotation direction (view from stern)		Clockwise
Design speed	(knots)	14.5

*1: These values are determined after the workshop. Please note that these values were not available in computations for the workshop

Fig. 1 Body plan of JBC

Table 2 Principal particulars of a model propeller

Diameter (mm)	203.0
Boss ratio	0.1800
Pitch ratio	0.7500
Expanded area ratio	0.5000
Max blade width ratio	0.2262
Blade thickness ratio	0.050
Angle of rake	5.00 deg
Number of blades	5
Blade section	MAU
Direction of rotation	Clockwise

2.3 Energy Saving Device

A circular duct installed ahead of a propeller is selected as an energy saving device, considering that a computational setup is easy due to its simple geometry. A duct is designed based on a parametric study using CFD simulations aiming to better propulsive efficiency. A series of computations are made for various configurations of ducts with diameters at trailing edge ranging from $0.70D_P$ to $1.10D_P$ where D_P is a diameter of a propeller, opening angles ranging from 5 deg. to 20 deg. and several vertical positions at model scale Reynolds number $R_n(L_{PP}) = 7.245 \times 10^6$. Final selection is made between two candidates based on self-propulsion test as shown below. Principal particulars of the designed duct are listed in Table 3. The duct is attached to the stern-tube using a vertical strut as shown in Fig. 2 in such a way that the leading edge of the duct is located at S.S. 1/4.

The geometry data of the hull, the propeller and the duct can be found at the Workshop web site (https://t2015.nmri.go.jp/).

Table 3 Principal particulars of a duct

Section	NACA4420
Diameter at trailing edge	$0.55D_P{}^{*1}$
Chord length	$0.3D_P{}^{*1}$
Opening angle	20 deg.

*1 D_P: propeller diameter
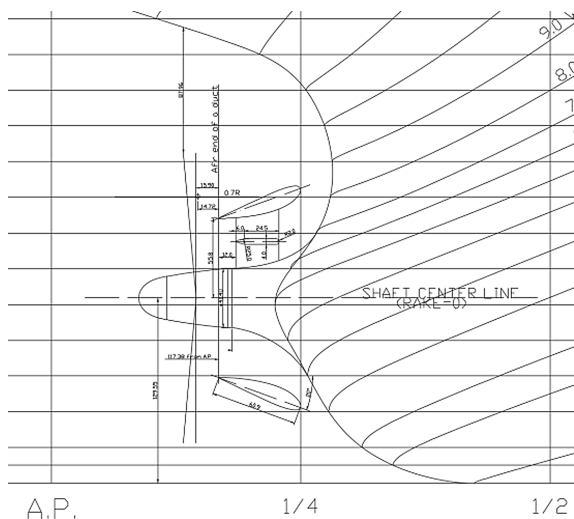
Fig. 2 Energy saving duct layout

2.4 Models

Three different models are used by National Maritime Research Institute, Japan (NMRI), Osaka University (OU) and Hamburg University of Technology (TUHH). Table 4 shows the principal particulars of each model used in three facilities. Two models of NMRI and OU are used in their tank tests (resistance and self-propulsion) and SPIV flow measurement. A model by TUHH is used to measure flow field by LDV and PIV in its wind tunnel. Note that the TUHH model is a double model shape. A rudder is not installed in all measurements to avoid interference with measuring

Table 4 Principal particulars of NMRI, OU and TUHH models

		NMRI	OU	TUHH
Length between perpendiculars	L_{PP}(m)	7.000	3.200	3.513
Length of waterline	L_{WL} (m)	7.125	3.257	3.576
Maximum beam of waterline	B_{WL} (m)	1.1250	0.5143	0.5646
Depth	D (m)	0.6250	0.2857	–
Draft	d (m)	0.4125	0.1886	0.2070
Wetted surface area w/o ESD	$S_{\_w/oESD}$ (m^2)	12.223	2.554	3.078
Wetted surface area with ESD	$S_{\_withESD}$ (m^2)	12.271	2.564	3/091
Block coefficient	C_B	0.8580		
Midship section coefficient	C_M	0.9981		
LCB ($\%L_{pp}$), fwd+		2.55		

instruments. Figures 3 and 4 are photographs of the NMRI model and the OU model, respectively. Figure 5 shows the TUHH model in the wind tunnel.
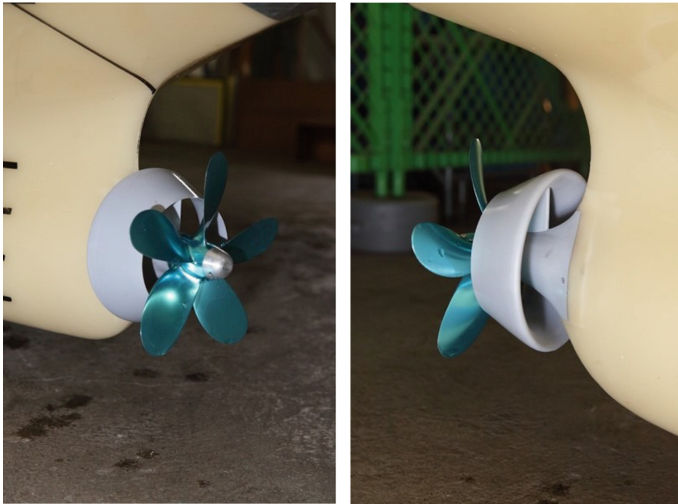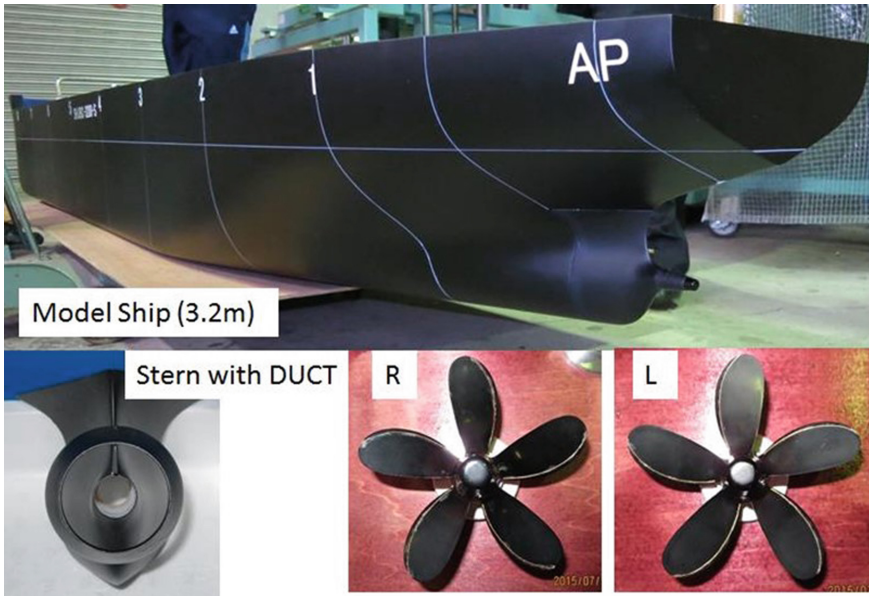

Fig. 3 NMRI model
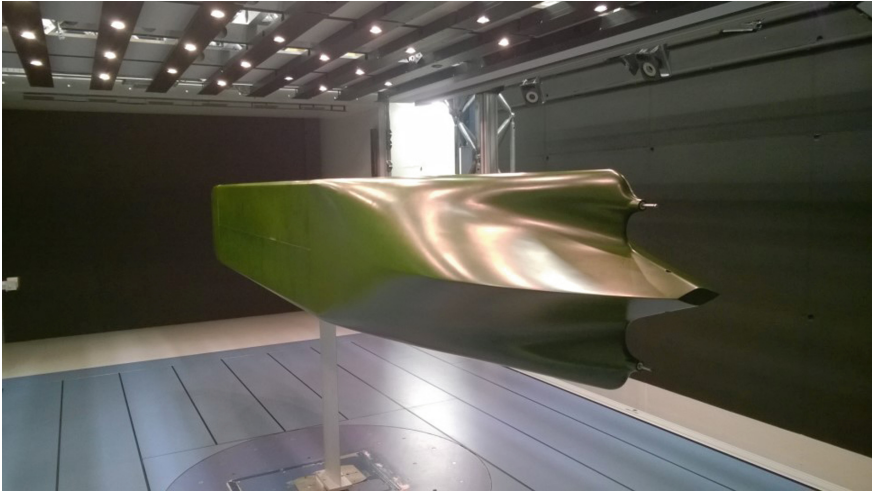

Fig. 4 OU model

Fig. 5 TUHH model

Model propellers used in self-propulsion tests and SPIV measurements at NMRI and OU are the MAU propeller shown in Table 3 with the diameters being 0.203 m for NMRI and 0.0928 m for OU, respectively. Propeller open water characteristics of the NMRI model propeller are shown in Fig. 6.
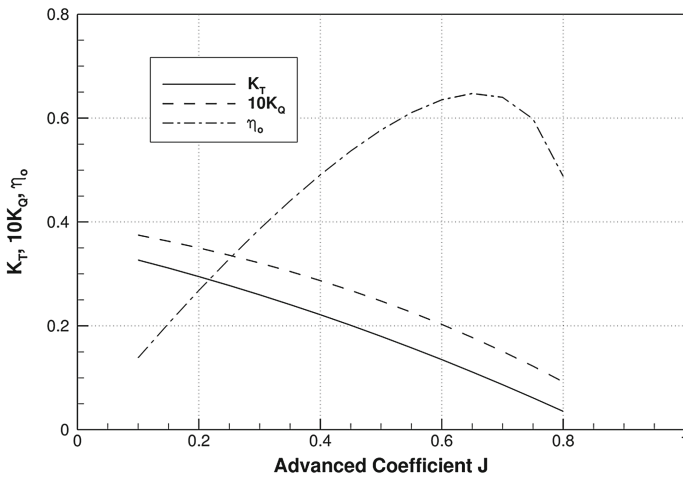
Fig. 6 Propeller open water characteristics of the NMRI model propeller

3 Resistance and Self-propulsion Tests

Resistance and self-propulsion tests are carried out in towing tanks of NMRI (Hino et al. 2016) and OU (Jufuku et al. 2015). The dimension (length, width and water depth) of tanks are $400 \times 18 \times 8$ m for NMRI and $100 \times 8 \times 4.35$ m for OU. The tests are conducted in the conditions with and without a duct while a rudder is not installed throughout the measurements.

The results at the design Froude number $F_n = 0.142$ are shown in Table 5 for both NMRI and OU. The form factors $1 + k$ are obtained using ITTC 1957 correlation line. Note that resistance coefficients of OU are based on the same wetted area (the value with the duct) for both configurations. The self-propulsion tests in both facilities are carried out at the ship point, where the roughness allowance ΔC_F is set to 0.12×10^{-3}.

NMRI data is obtained at the Reynolds number $R_n = 7.569 \times 10^6$ for both with and without the duct. However, test cases 1.1a and 1.2a of T2015 Workshop adopted $R_n = 7.46 \times 10^6$, the same as the SPIV measurement. This makes it possible to use the same computations between cases for integral values and for local flow data. On the other hand, the C_T, K_T, K_Q or propeller revolution values given as the validation data at the Workshop are slightly different (approximately 0.3% in case of C_T) from the values with specified Reynolds number. Nevertheless, this difference is within the nominal uncertainty of the resistance tests (1% D).

Table 5 Results of resistance and self-propulsion tests at design speed

	NMRI		OU	
ESD	Without Duct	With Duct	Without Duct	With Duct
V_m(m/s)	1.179	1.179	0.795	0.795
$F_n(L_{pp})$	0.142	0.142	0.142	0.142
$R_n(L_{pp})$	7.569×10^6	7.569×10^6	2.17×10^6	2.17×10^6
C_T	4.29×10^{-3}	4.26×10^{-3}	5.27×10^{-3}	5.28×10^{-3}
$1 + k$	1.314	1.305	1.26	1.26
C_w	1.50×10^{-4}	1.52×10^{-4}	2.447×10^{-4}	2.547×10^{-4}
sinkage/L_{PP}(%)	-8.57×10^{-2}	-8.46×10^{-2}	-7.65×10^{-2}	-7.45×10^{-2}
trim/L_{PP}(%)	-1.80×10^{-1}	-1.82×10^{-1}	-1.75×10^{-1}	-1.75×10^{-1}
n(1/s)	7.810	7.516	11.8	11.8
K_T	0.217	0.233	0.217	0.230
$10K_Q$	0.279	0.295	–	–
$1 - t$	0.804	0.810	0.748	0.751
$1 - w_T$	0.552	0.481	0.400	0.346
η_R	1.015	1.009	–	–

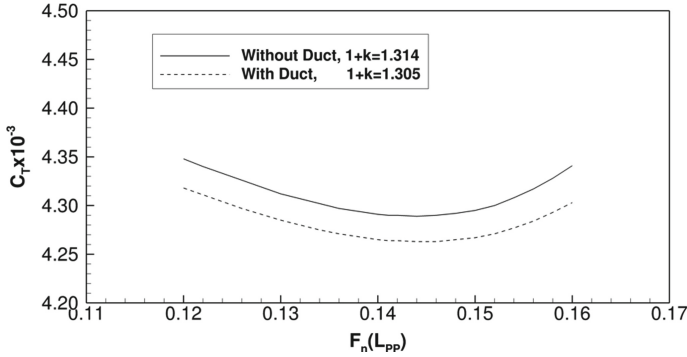Sinkage is positive upward and trim is positive bow up

Fig. 7 Total resistance coefficient (C_T) of NMRI model

Figures 7 through 10 show all the measured results of resistance tests at NMRI. Figure 7 shows total resistance coefficient $\left(C_T = \frac{R_T}{0.5\rho U_0^2 S}\right)$ curves of the cases with and without the duct. C_T with the duct is smaller than that without the duct at every Froude number, while wave making resistance coefficient $\left(C_W = \frac{R_W}{0.5\rho U_0^2 S}\right)$ curves shown in Fig. 8 are not so different between with and without the duct. Trim and sinkage are shown in Figs. 9 and 10, respectively. Trim τ and sinkage σ are defined as $\tau = (d_a - d_f)/L_{pp}$ and $\sigma = -(d_a + d_f)/2L_{pp}$, where d_f and d_a are dipping at FP and AP, respectively. Differences of trim and sinkage between with and without duct are very small.

Figures 11 through 15 are the results of self-propulsion tests at NMRI in which a range of Froude numbers from 0.12 to 0.16 are covered. The thrust deduction coefficient $1 - t$ in Fig. 11 and relative rotative efficiency η_R in Fig. 13 show small differences between with and without the duct. $1 - t$ is larger with the duct than without the duct, while η_R shows the opposite trend. $1 - w_T$ with w_T being wake
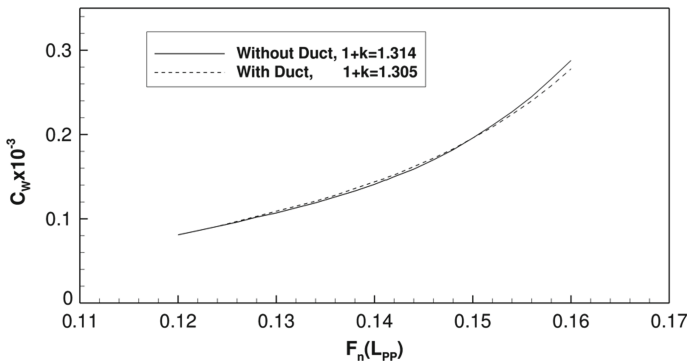

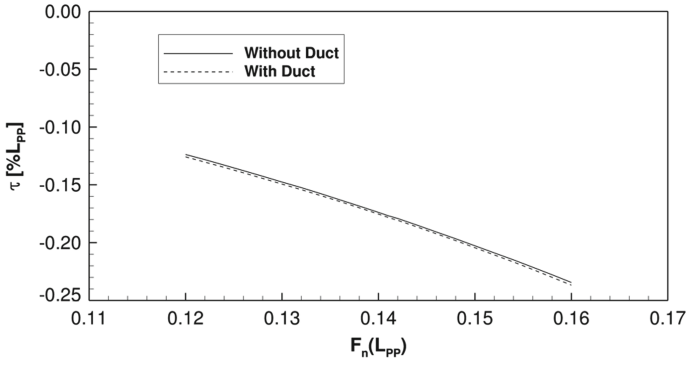**Fig. 8** Wave making resistance coefficient (C_W) of NMRI model
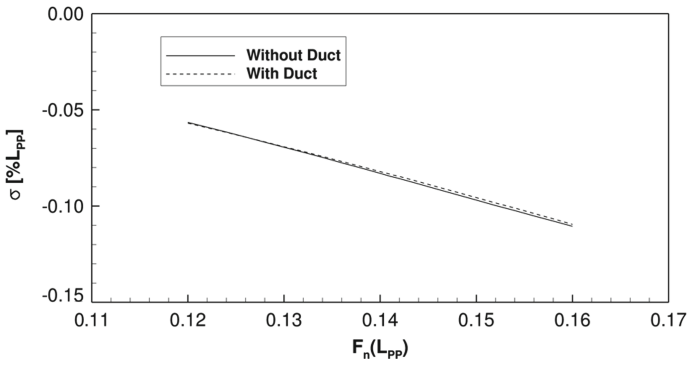
Fig. 9 Trim of NMRI model
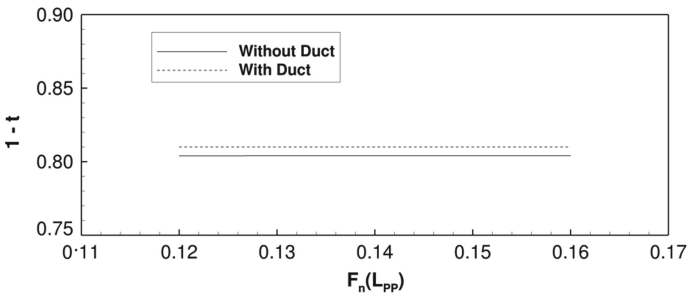

Fig. 10 Sinkage of NMRI model

Fig. 11 Thrust deduction coefficient $(1 - t)$ of NMRI model

fraction is largely improved by the presence of the duct as shown in Fig. 12. Both K_T in Fig. 14 and K_Q in Fig. 15 increase with the duct.
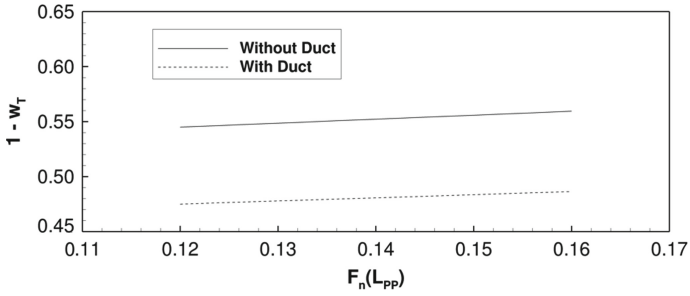
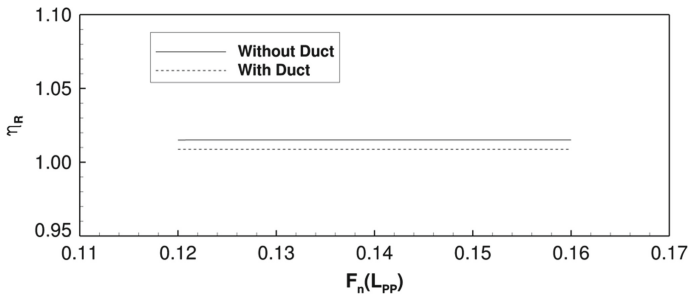**Fig. 12** Thrust wake coefficient $(1 - w_T)$ of NMRI model

Fig. 13 Relative rotative efficiency (η_R) of NMRI model
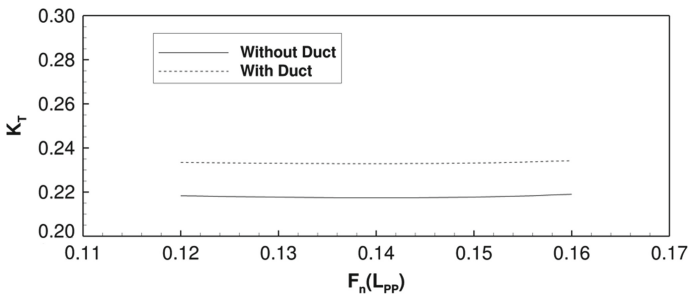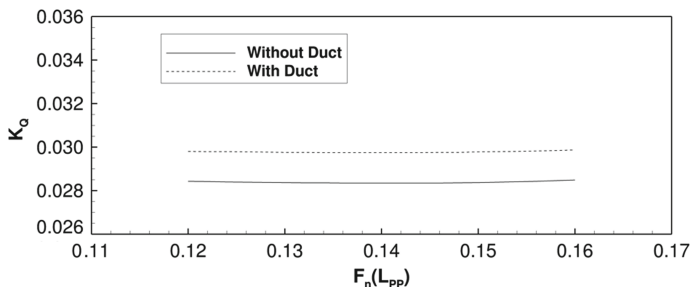

Fig. 14 Propeller thrust coefficient (K_T) of NMRI model

4 Detailed Flow Measurements

4.1 Overview

For the validation of computed results, not only the integrated values such as C_T, the attitude of the hull and self-propulsion factors but also detailed flow field data are desired. To this end, Stereo Particle Image Velocimetry (SPIV) measurements

Fig. 15 Propeller torque coefficient (K_Q) of NMRI model

are carried out at the towing tanks of NMRI (Hino et al. 2016) and OU (Jufuku et al. 2015). Also, LDV/PIV measurement is conducted at the TUHH wind tunnel (Shevchuk et al. 2020).

The models used in NMRI, OU and TUHH measurements are specified in Table 4. Measuring sections are common in three facilities. Seven cross sections with constant x/L_{PP} ahead and behind a duct ranging from S.S. 1/2 to AP are adopted as shown in Fig. 16 for NMRI measurements. Section 1 (S1) is at S.S. 1/2 ($x/L_{PP} = 0.950$), Sect. 2 (S2) at S.S. 3/8 ($x/L_{PP} = 0.9625$), Sect. 3 (S3) is at the duct mid-chord ($x/L_{PP} = 0.9788$), Sect. 4 (S4) is between the duct and the propeller ($x/L_{PP} = 0.9843$), Sect. 5 (S5) is at the propeller plane ($x/L_{PP} = 0.9864$), Sect. 6 (S6) is behind the propeller boss ($x/L_{PP} = 0.9923$) and Sect. 7 is at AP ($x/L_{PP} = 1.0000$).

The measurement in NMRI is carried in its middle towing tank (length $\times$ width $\times$ depth $= 150 \times 7.5 \times 3.5$ m) using 7.0 m model, while that in OU is done in its towing tank (length $\times$ width $\times$ depth $= 100 \times 8 \times 4.35$ m) using 3.2 m model. Froude number is $F_n = 0.142$ in both NMRI and OU measurements. Reynolds numbers are 7.46×10^6 and 2.17×10^6 in NMRI and OU, respectively.

LDV/SPIV measurement is conducted in the TUHH wind tunnel. The TUHH low-speed wind tunnel is 40 m long with the test section (length $\times$ width $\times$ height $= 5.5 \times 3 \times 2$ m). The double model of length 3.513 (m) is used and the blockage coefficient is 0.04. The wind velocity $U_0 = 11.8$ m/s which corresponds to Reynolds number of 2.74×10^6 for LDV measurement and $U = 10.0$ m/s and Reynolds number of 2.42×10^6 for SPIV measurement.

4.2 Accuracy Estimation of SPIV Measurement at NMRI

The uniform flow measurements without a ship model using SPIV system are conducted at NMRI for clarification of the accuracy. Figure 17 shows the measured data of uniform flow at $U_0 = 1.0$ m/s which consists of three-components of velocity u, v and w and turbulent kinetic energy TKE. The accuracy of the averaged velocities can be estimated to be $2-3\%$ of U_0 for u, $3-4\%$ of U_0 for v and 1% of U_0 for w.
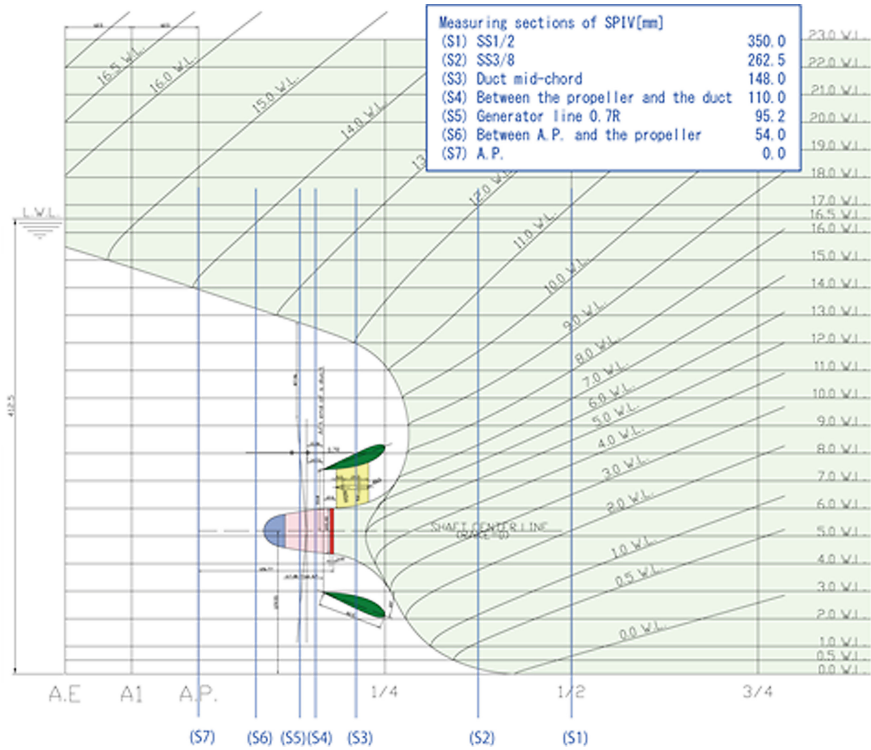
Fig. 16 Measuring sections of velocity fields

The reason why the accuracy of v is somewhat large is that the reflection mirror in the PIV system is not adjusted correctly. For the accuracy of TKE, $0.3-0.5\%$ of U_0^2 can be estimated. Note that all the data is acquired using 250 images.

To assess the accuracy of NMRI measurement further, the statistical convergence of PIV data is examined. Measurement at the S4 section without a propeller and without a duct is taken as an example. Figure 18 is the contours of the axial velocity u and TKE k, respectively, measured at NMRI. Figure 19 is the cumulative moving errors of velocity components and TKE with respect to the number of images. Figure 20 is the histogram of three velocity components. Figure 21 shows the statistical convergence errors of the mean velocity components and TKE. The sample point is at $y/L_{PP} = -0.009814$ and $z/L_{PP} = -0.03926$ also shown as a red circle in Fig. 18. The velocity components and the TKE values in Fig. 19 do not converge completely since the number of images is limited to about 1000, though the data variations are small. The histograms in Fig. 20 show that the fluctuations of velocity components are large. This may be also due to the small number of images. The statistical convergence of the mean velocity components in Fig. 21 is defined using the sample standard deviation s_x as
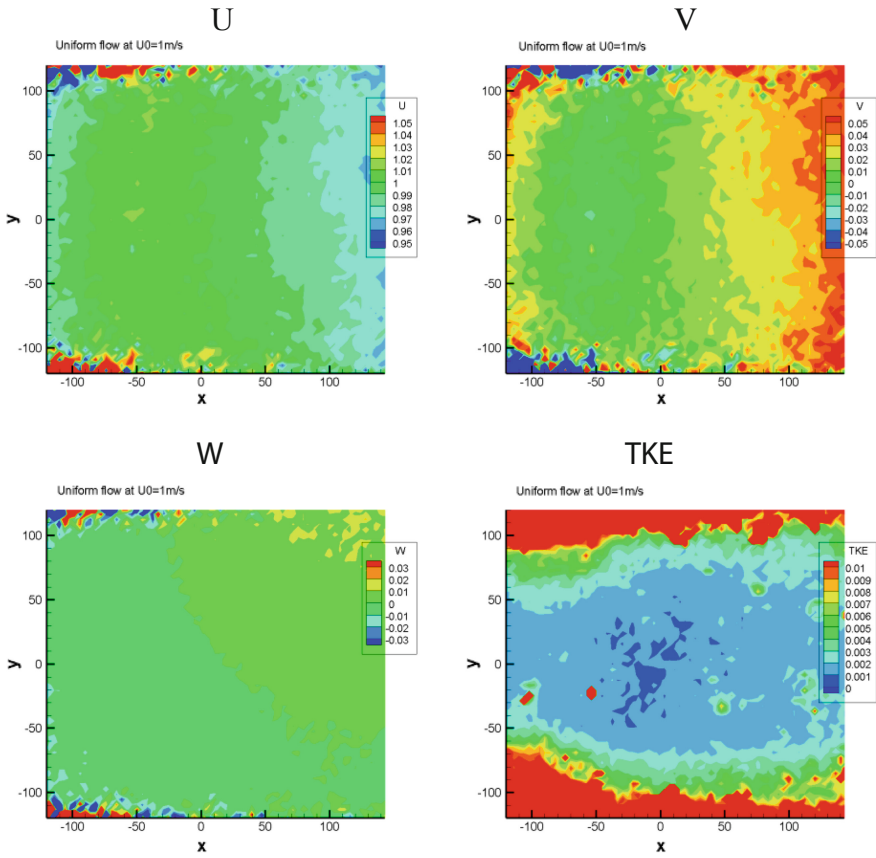
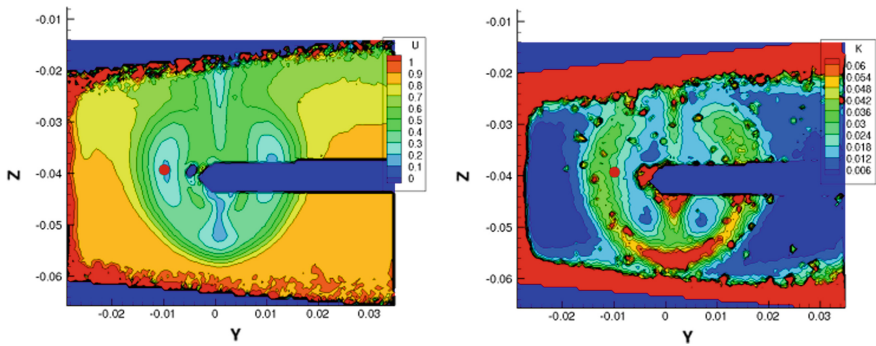**Fig. 17** SPIV measurement of uniform flow ($U_0 = 1.0$ m/s) at NMRI

Fig. 18 Contours of the axial velocity u (left) and TKE k (right) in S4 ($x/L_{PP} = 0.9843$) station of NMRI measurement
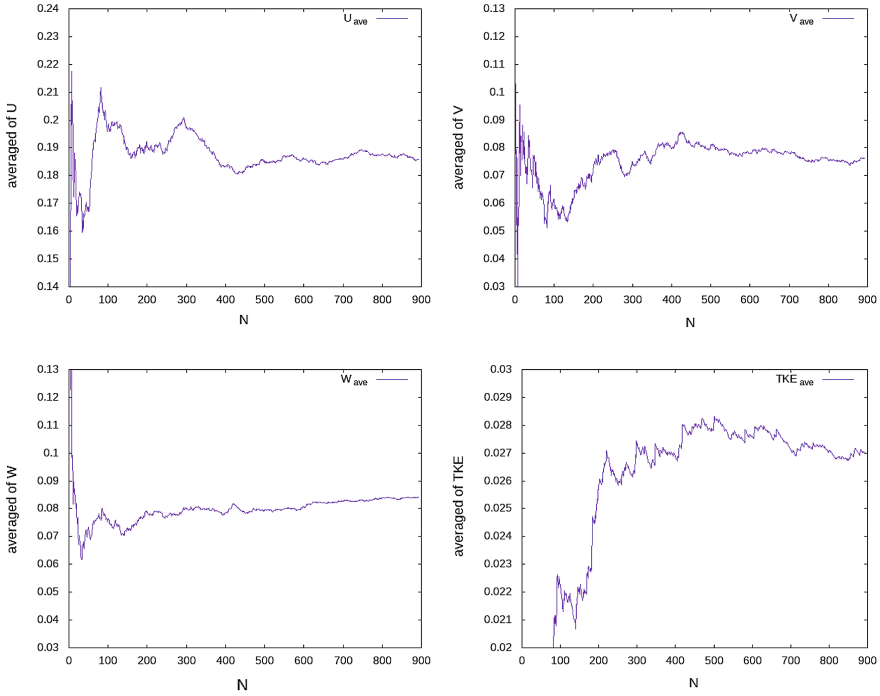
Fig. 19 Cumulative moving averages of velocity components and TKE in NMRI measurement
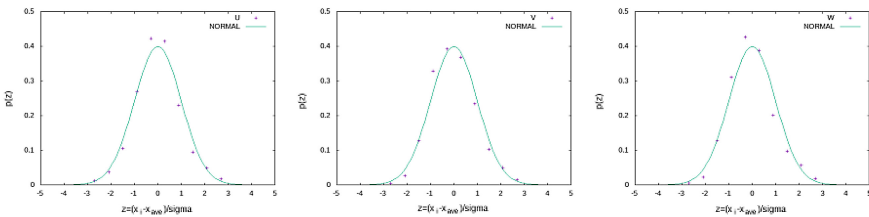

Fig. 20 Histogram of velocity components in NMRI measurement

$$E_{SC}(\%) = \frac{t_{n;\alpha/2}}{\sqrt{N}} \frac{s_x}{x_{\text{ref}}} \times 100$$

where N is the sample size and $t_{n;\alpha/2}$ is the Student-t variable of $n = N-1$ degrees of freedom for a $100(1-\alpha)$ percent level of confidence and x_{ref} is the reference velocity equal to the uniform flow magnitude, U_0 (Yoon et al. 2015). For the convergence of TKE, the χ^2-distribution is assumed and the upper and lower limits of the confidence interval is defined based on the sample variance s_x^2 as
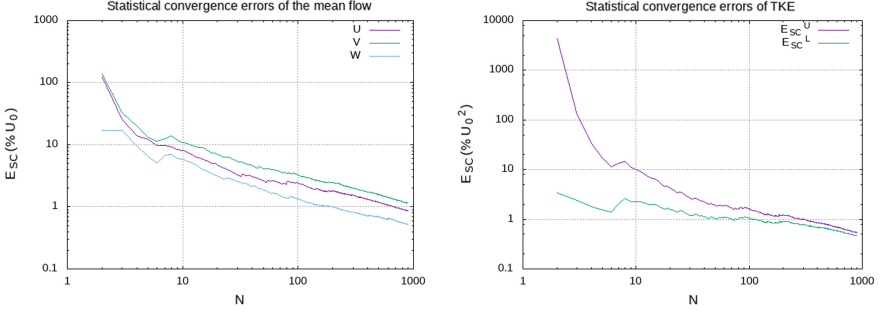
Fig. 21 Statistical convergence errors of mean velocity components (left) and TKE (right) at in NMRI measurement at and $(y/L_{pp}, z/L_{pp}) = (-0.009814, -0.03926)$

$$E_{SC}^{U} \; (\%) \; = \; \left(\frac{n}{\chi_{n;1-\alpha/2}^{2}} - \right) \frac{s_x^2}{s_{ref}^2} \; \times \; 100$$

$$E_{SC}^{L} \; (\%) \; = \; \left(1 - \frac{n}{\chi_{n;\alpha/2}^{2}} \right) \frac{s_x^2}{s_{ref}^2} \; \times \; 100$$

for a $100(1-\alpha)$ percent level of confidence. The $\chi_{n;1-\alpha/2}^2$ and $\chi_{n;\alpha/2}^2$ are the χ^2 variables and s_{ref}^2 is the reference velocity-squared value for which the square of the uniform velocity magnitude U_0^2 is taken (Yoon et al. 2015). Note that 95% level of confidence ($\alpha = 0.05$) is set for all variables. When the sample size N is approaching to 1000, the statistical convergence of the mean velocity component is around 1% of U_0 and that of TKE is below 1% of U_0^2. Figure 22 depicts the contours of the statistical convergence errors E_{SC} for the mean velocity components and E_{SC}^U for TKE in the S4 section. The convergence error of the mean velocity u, v and w are proportional to their standard deviations which correspond to the square-root of the normal Reynolds stresses, $\sqrt{u'u'}$, $\sqrt{v'v'}$ and $\sqrt{w'w'}$. The patterns, therefore, are similar to that of TKE in Fig. 18. The error levels of u, v and w are estimated as 1.2, 1.4 and 0.6% of U_0 for the average and 1.8, 2.0 and 0.9% of U_0 for the maximum, respectively. The error of TKE is 1.0% of U_0^2 for the average and 1.6% of U_0^2 for the maximum. The errors of v are slightly larger than those of u, which is also observed in Fig. 22. Though the reason is not clear, it may be related to the mirror alignment problem.

Total uncertainty of PIV measurement is estimated using the analysis above. The bias errors E_b are estimated from the uniform flow test and the precision errors E_p from the statistical convergence errors and the uncertainty is defined as $\sqrt{E_b^2 + E_p^2}$. Results are shown in Table 6 and the average uncertainty of the mean velocity is $1-3\%$ of U_0 and that of TKE is 1.0% of U_0^2. The maximum uncertainty is slightly larger than the average.
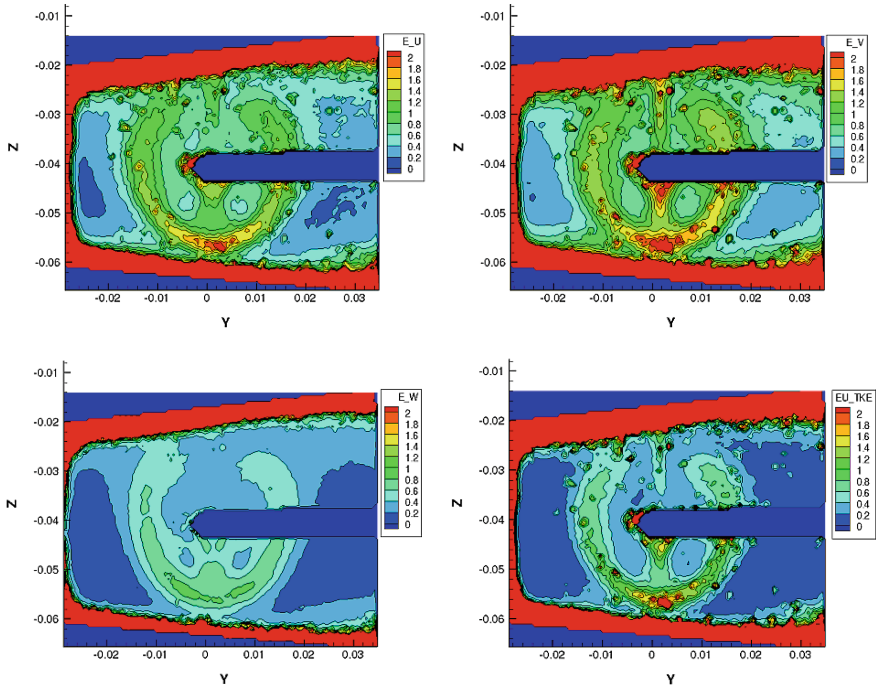
Fig. 22 Contours of the statistical convergence errors mean velocity u (top left), v (top right), w (bottom left) and TKE k (bottom right) in S4 ($x/L_{pp} = 0.9843$) station of NMRI measurement

Table 6 Uncertainty of PIV measurement

|	Bias error	Precision error (average)	Precision error (max.)	Uncertainty (average)	Uncertainty (max.)
u (%U_0)	2.0	1.2	1.8	2.3	2.7
v (%U_0)	3.0	1.4	2.0	3.3	3.6
w (%U_0)	1.0	0.6	0.9	1.2	1.3
TKE (%U_0^2)	0.3	1.0	1.6	1.0	1.6

4.3 Credibility of SPIV Measurement at NMRI, OU and TUHH

In order evaluate the credibility of measurement, the measured data of three facilities are compared. The test case 1.3 in the workshop, i.e. the towed condition without a propeller and without an ESD is chosen since this configuration is simplest.
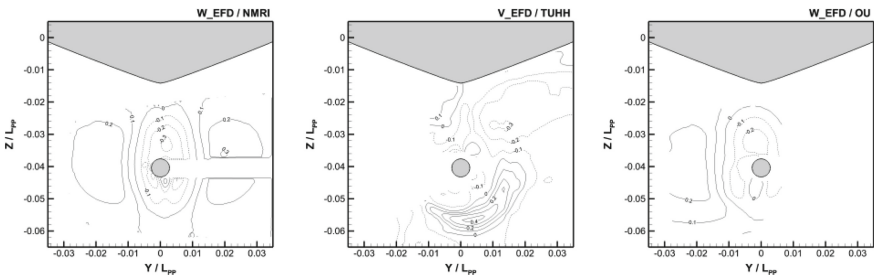
In the S4 section ($x/L_{PP} = 0.9843$), the contours of the axial velocity u, the horizontal velocity v and the vertical velocity w are shown in Figs. 23, 24 and 25,
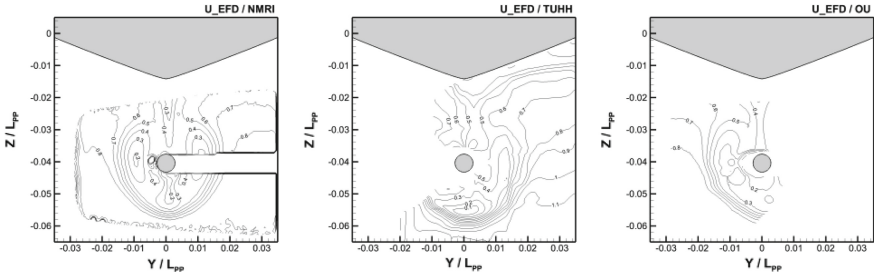
Fig. 23 Contours of measured axial velocity (*u*) at S4 section. Left: NMRI, middle: TUHH and right: OU
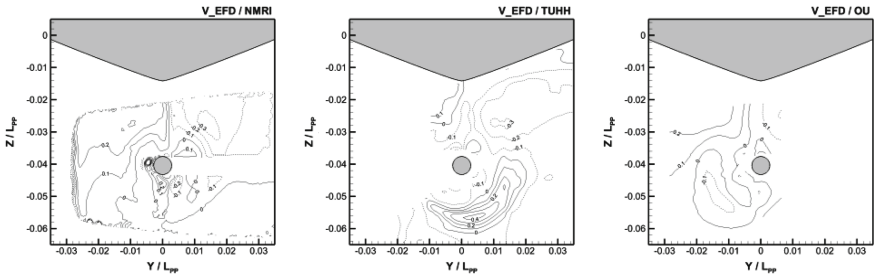
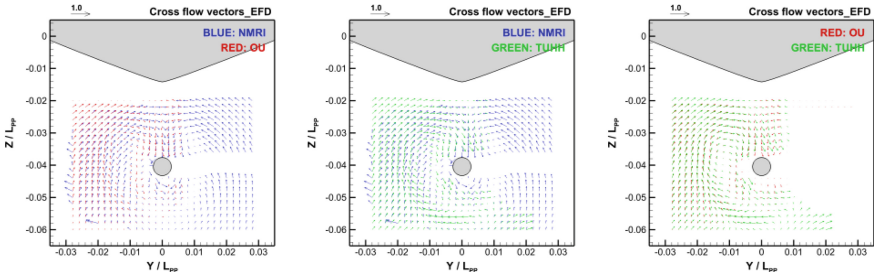**Fig. 24** Contours of measured horizontal velocity (*v*) at S4 section. Left: NMRI, middle: TUHH and right: OU

Fig. 25 Contours of measured vertical velocity (*w*) at S4 section. Left: NMRI, middle: TUHH and right: OU

respectively. Comparisons of the crossflow vectors are shown in Fig. 26 and contours of the *x*-vorticity ω_x and TKE *k* are shown in Figs. 27 and 28, respectively.

All the velocity contours are similar to each other and the so-called hook shapes can be observed. While NMRI data is almost symmetric in *y* direction, the measured areas of TUHH and OU are too narrow to exhibit symmetry.

Lateral locations of the longitudinal vortices of OU and TUHH are almost same. That of NMRI, on the other hand, is a little closer to a symmetry plane. This is due

Fig. 26 Comparisons of cross flow vectors (v, w) at S4 section. Left: NMRI/OU, middle: NMRI/TUHH and right: OU/TUHH

Fig. 27 Contours of measured vorticity (ω_x) at S4 section. Left: NMRI, middle: TUHH and right: OU

Fig. 28 Contours of measured turbulent kinetic energy (k) at S4 section. Left: NMRI, middle: TUHH and right: OU
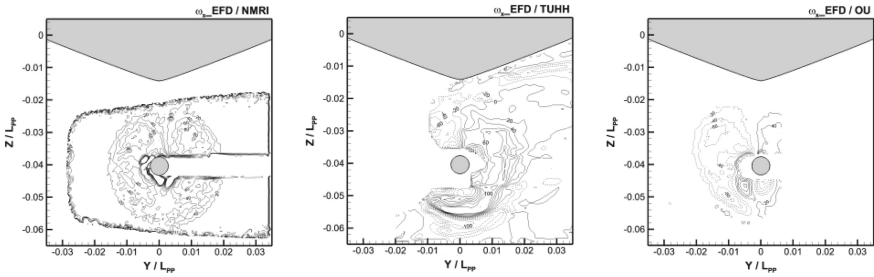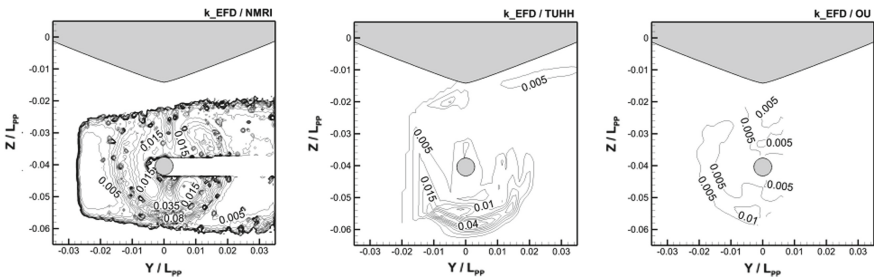
to the difference of Reynolds numbers. Reynolds numbers of OU and TUHH are almost the same, 2.17×10^6 and 2.42×10^6, respectivley, and that of NMRI is larger, 7.46×10^6. It is known that the boundary layer is thicker in low Reynolds number flows.

In the narrow region near the center of measuring area ($-0.01 < y/L_{PP} < 0.01$, $-0.05 < z/L_{PP} < -0.03$), axial and horizontal velocities u and v agree well between NMRI and OU. However, the discrepancies between NMRI and OU become large in

| y/L_{PP} | > 0.015 and the crossflow vectors of NMRI data in Fig. 26 are inclined to the positive y direction. This is due to the problem of the reflection mirror in NMRI's SPIV system as described above. The uniform flow measurement in Fig. 17 indicates v is overestimated by about 5% of uniform velocity $U_0 = 1.00$ m/s near both side edges of the measuring area. In TUHH case, all flow components under the propeller shaft show asymmetric distributions which is due to the laser reflection effects. The contours of x-vorticity ω_x in Fig. 27 are similar between NMRI and OU. TUHH data is different from the other two, particularly under the propeller shaft, which is again attributed to the laser reflection. The distributions of TKE in Fig. 28 show that the peak value of NMRI data is much larger than that of OU, although the patterns are similar. Figures 29 through 34 are the same plots in the S7 section as Figs. 23 through 28 in the S4 section. General trends are the same in case of the S4 section.

The large differences are found in the TKE distributions between NMRI and OU as shown in Figs. 28 and 34. The convergence of TKE data is shown in Fig. 19 for NMRI case and it exhibits the reasonable convergence with 1000 images. TKE of OU data is acquired using 3000 images and it is believed the convergence is similar or better than NMRI data. Therefore, the difference of TKE values between NMRI and OU seems to come from the reason other than the statistical convergence though more images may be needed for the accurate measurement of turbulent quantities.
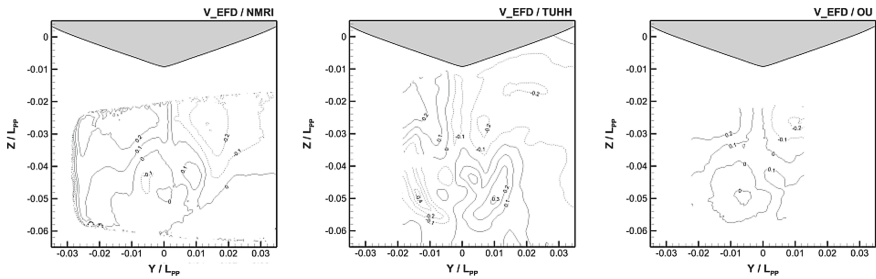

Fig. 29 Contours of measured axial velocity (u) at S7 section. Left: NMRI, middle: TUHH and right: OU
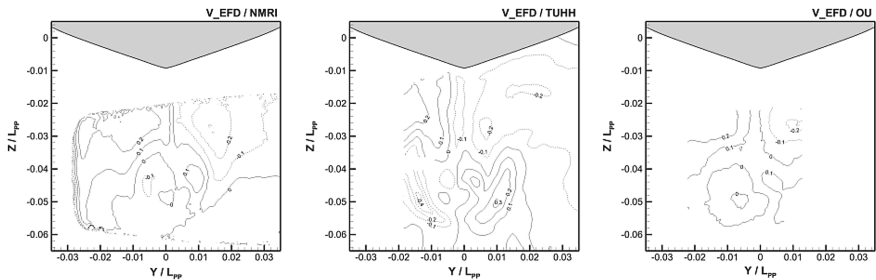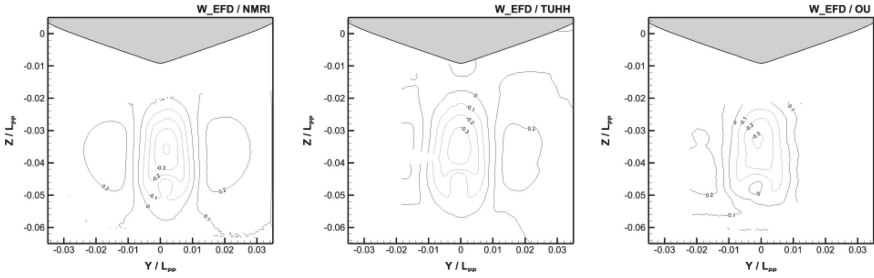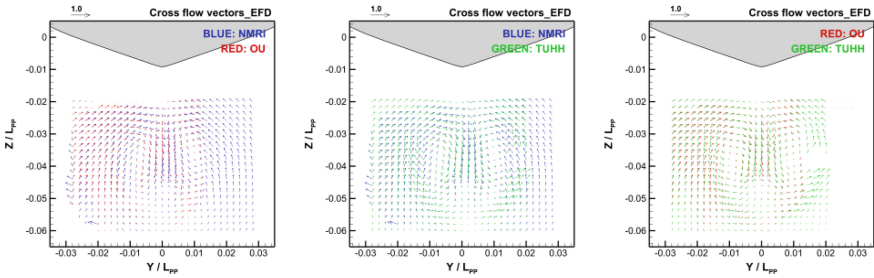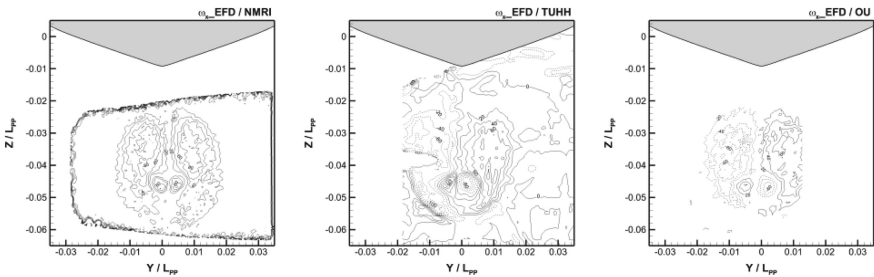

Fig. 30 Contours of measured horizontal velocity (v) at S7 section. Left: NMRI, middle: TUHH and right: OU

Fig. 31 Contours of measured vertical velocity (*w*) at S7 section. Left: NMRI, middle: TUHH and right: OU

Fig. 32 Comparisons of cross flow vectors (*v*, *w*) at S7 section. Left: NMRI/OU, middle: NMRI/TUHH and right: OU/TUHH

Fig. 33 Contours of measured vorticity (ω_x) at S7 section. Left: NMRI, middle: TUHH and right: OU

In order to assess the Reynolds number effect, three TKE data are compared by the scaled variables. TKE distributions along the horizontal line at the shaft height shown in Fig. 35 are extracted from NMRI, OU and TUHH measurement. The distributions are plotted as $\sqrt{\text{TKE}}/u_\tau \sim y^+$ in left of Fig. 35. Also plotted is the same scaled data from the propeller plane of KVLCC2. The data is taken from the wind tunnel measurement by a hot-wire (Lee et al. 2003) where Reynolds number is $R_n = 4.6 \times 10^6$. The wall distance *y* is measured from the shaft edge and the friction
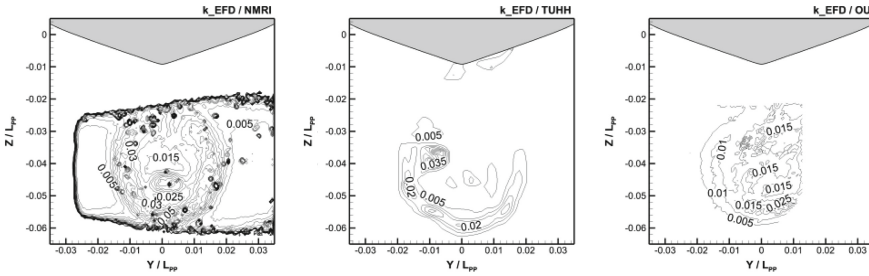
Fig. 34 Contours of measured turbulent kinetic energy (*k*) at S7 section. Left: NMRI, middle: TUHH and right: OU
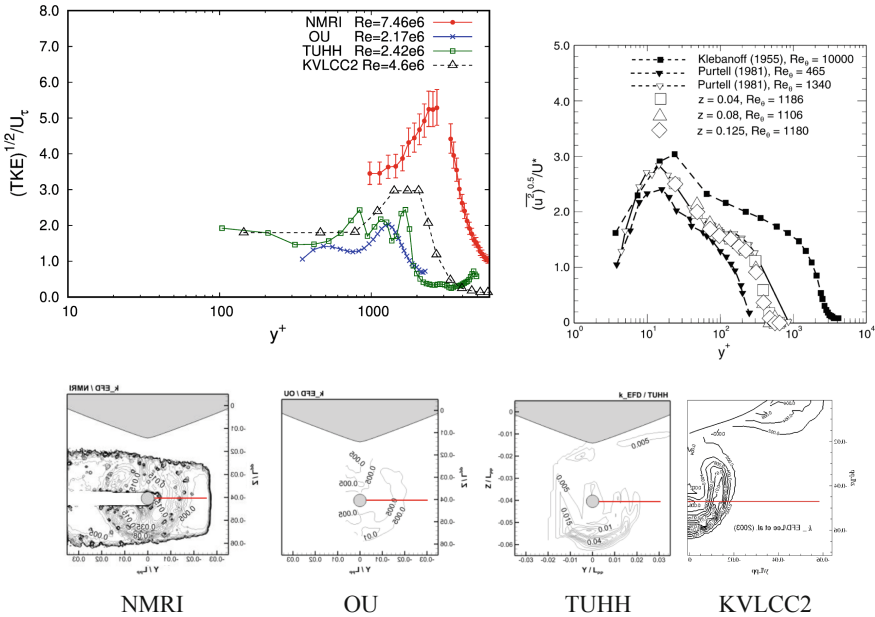
Fig. 35 Left: Distributions of scaled TKE along a horizontal line at the shaft height in S4 section of JBC and the propeller plane of KVLCC2. Right: Distributions of scaled streamwise normal Reynolds stress $\overline{u'u'}$ of a flat plate boundary layer (Longo et al. 1998). Bottom: Data-extracted lines

velocity u_τ is estimated from the local c_f of a turbulent boundary layer of a flat plate using the formula of Prandtl- Schlichting as below

$$c_f = (2.0 \log_{10}(Re_x) - 0.65)^{-2.3}, \quad u_\tau/U = \sqrt{c_f/2}$$

where Re_x is set equal to the Reynolds number of each case. Actual data of u_τ/U_0 in each case are 0.0367, 0.0405, 0.0401 and 0.0381 for NMRI, OU, TUHH and KVLCC2, respectively. The plots show the similarity in the distribution patterns of

all cases. Note that the irregular data of NMRI measurement are omitted. The peak locations and peak values of OU and TUHH are almost the same since the Reynolds numbers of two cases are similar. The peak value of NMRI is larger than those of OU and TUHH. KVLCC2 data with the moderate Reynolds number is in-between OU/TUHH and NMRI for the peak location and value. Right of Fig. 35 is the scaled streamwise normal Reynolds stress $\overline{u'u'}$ in the boundary layer (Longo et al. 1998). The distributions show the different distribution pattern than the JBC case, though the general tendency of the turbulence increase with Reynolds number seems to be the same as in the JBC case.

Figure 36 shows the maximum TKE values of $k^+ (= k/u_\tau^2)$ in the profiles of the present horizontal lines. Again, the peak values of TKE increase with the Reynolds number. The NMRI data has the highest peak value but it is rather difficult to tell if this follows the trend of the other data or not since the date points is quite few.

Figure 37 shows the wake-scale distributions of u velocity. The wake half width b is determined by manual fitting of the velocity distributions. Due to the presence of the vortex core, the velocity distributions have the minimum away from the center. The TKE distributions in the wake-scale are shown in left of Fig. 38. Right of Fig. 38 is the similar plot for the wake of a flat plate (Longo et al. 1998). The distributions of the JBC case look closer to the wake profiles rather than the boundary layer profiles in Fig. 35.

In summary, it is rather difficult to assess the quantitative Reynolds number effect from the data currently available. Although the tendencies seem to be reasonable, the extremely higher peak of NMRI data compared with other cases cannot be fully justified. Further investigations, such as additional measurements in different facilities and/or different measuring systems, are desirable for obtaining the proper distributions of TKE.
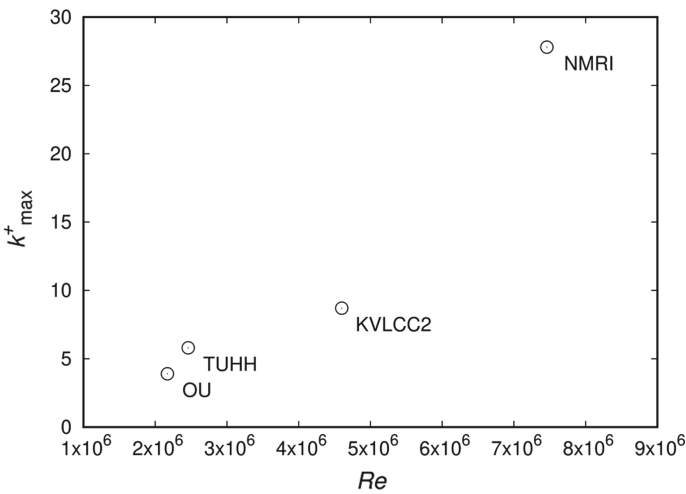
Fig. 36 Relation of R_n and the maximum TKE k^+
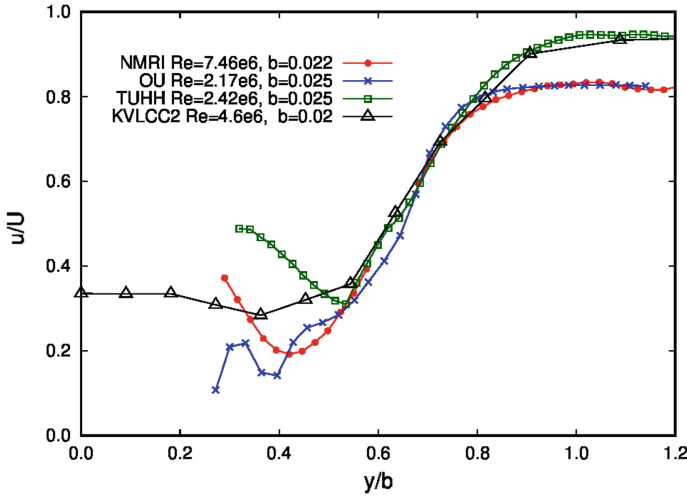
Fig. 37 Wake-scale distribution of *u* velocity along a horizontal line at the shaft height in S4 section shown in Fig. 35
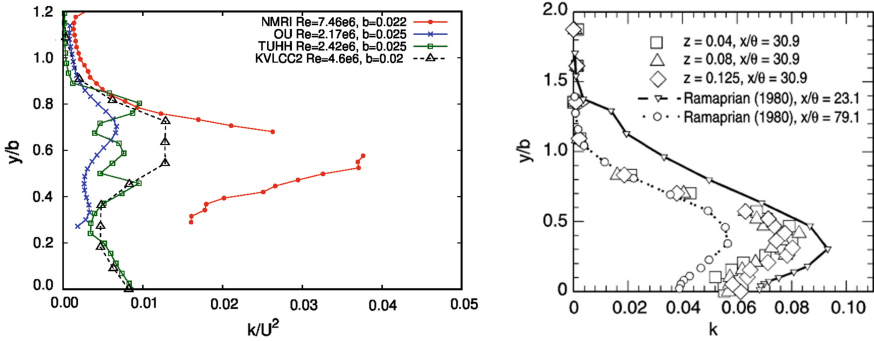
Fig. 38 Left: Wake-scale distribution of TKE along a horizontal line at the shaft height in S4 section shown in Fig. 35. Right: Distributions of turbulent kinetic energy in the wake of a flat plate (Longo et al. 1998)

On the other hand. for the mean velocity components, the data of three facilities are generally in good accordance. However, TUHH measurement has the problem of laser reflection under the propeller shaft and NMRI data has some errors (about $3-4\%$ of the uniform axial velocity) in *v* near the side edges of measuring area though the errors can be negligible in the center. In total, the OU data seems to have no serious deficiencies and thus this can be considered as the reliable measured data.

Table 7 Test cases of JBC local flow fields

Test case	Conditions
Cases1.3a and 1.3b	Towed in calm water condition w/o rudder w/o propeller and w/o ESD
Case1.4a	Towed in calm water condition w/o rudder w/o propeller and with ESD
Case1.7a	Self-propelled at the ship point in calm water w/o rudder, with propeller and w/o ESD
Case1.8a	Self-propelled at the ship point in calm water w/o rudder, with propeller and with ESD

4.4 Local Flow Data of NMRI, OU and TUHH Used in Test Cases

In the Workshop, the test cases for local flow fields are set up as Table 7 based on the measurement described above. SPIV data of the measuring sections S2, S4 and S7 shown in Fig. 16 are picked up for all the test cases. Cases 1.3 and 1.4 are towed condition without and with ESD, respectively. Similarly, Cases 1.7 and 1.8 are the self-propelled condition without and with ESD. Note that the NMRI data were used for all the cases with the identification "a" and the part of the TUHH data of LDV measurement was used in Test Case 1.3b. The OU data and SPIV data of TUHH were not used in the Workshop. All the data both used and not used in the Workshop are listed in Table 8. In Cases 1.7 and 1.8 with a rotating propeller, 'averaged' indicates the mean flow data and 'prop000' to 'prop048' indicate the phase averaged data with the blade angles of 0 to 48 degrees, respectively. Actual figures of the data used in the Workshop data are shown in Chap. 6 together with the submitted numerical results.

5 Wave Height Measurement

Wave height distributions around JBC advancing at the design speed $F_n = 0.142$ are measured in the large towing tank of NMRI. The ship is towed in a trim-free condition without a propeller and a duct. The wave profile on the hull is acquired from the photographs of the hull surface on which the ordinate and the abscissa are marked. The longitudinal wave cuts are measured using the capacitance type wave gauge at $y/L_{PP} = 0.1043$ and 0.1900 where y is the lateral distance from the center line of the hull. Figure 39 shows the wave profile on the hull. Figures 40 and 41 show the longitudinal wave cuts at $y/L_{PP} = 0.1043$ and 0.1900, respectively.

Table 8 List of local veocity data

Testcase	Section	Flow variables	NMRI	TUHH/LDV	TUHH/SPIV	OU
Case1.3	S2	u, v, w	O			*
		ω_x , k	O			*
	S4	u, v, w	O	O	*	*
		ω_x , k	O		*	*
	S7	u, v, w	O	O	*	*
		ω_x , k	O		*	*
Case1.4	S2	u, v, w	O			*
		ω_x , k	O			*
	S4	u, v, w	O			*
		ω_x , k	O			*
	S7	u, v, w	O			*
		ω_x , k	O			*
Case1.7 Averaged	S2	u, v, w	O			*
Case1.7 prop000	S4	u, v, w	O			*
Case1.7 prop024	S4	u, v, w	O			*
Case1.7 prop048	S4	u, v, w	O			*
Case1.7 Averaged	S4	u, v, w	O			*
Case1.7 prop000	S7	u, v, w	O			*
Case1.7 prop024	S7	u, v, w	O			*
Case1.7 prop048	S7	u, v, w	O			*
Case1.7 Averaged	S7	u, v, w	O			*
Case1.8 Averaged	S2	u, v, w	O			*
Case1.8 prop000	S4	u, v, w	O			*
Case1.8 prop024	S4	u, v, w	O			*
Case1.8 prop048	S4	u, v, w	O			*
Case1.8 Averaged	S4	u, v, w	O			*
Case1.8 prop000	S7	u, v, w	O			*
Case1.8 prop024	S7	u, v, w	O			*
Case1.8 prop048	S7	u, v, w	O			*
Case1.8 Averaged	S7	u, v, w	O			*

O: data used in the Workshop *: data not used in the Workshop

6 Conclusions

In this Chapter, the measured data for Japan Bulk Carrier (JBC) with an energy saving circular duct are presented. The measurement is conducted in three facilities, i.e., the towing tanks of National Maritime Research Institute (NMRI) and Osaka University (OU) and the wind tunnel of Hamburg University of Technology (TUHH).
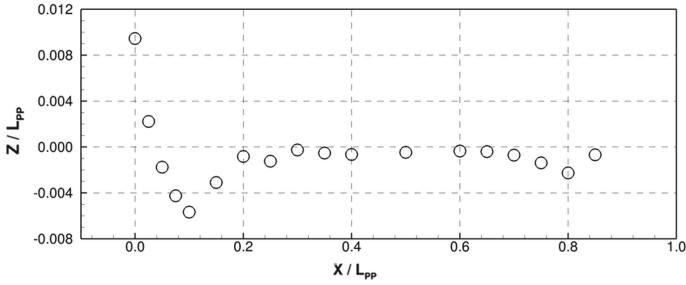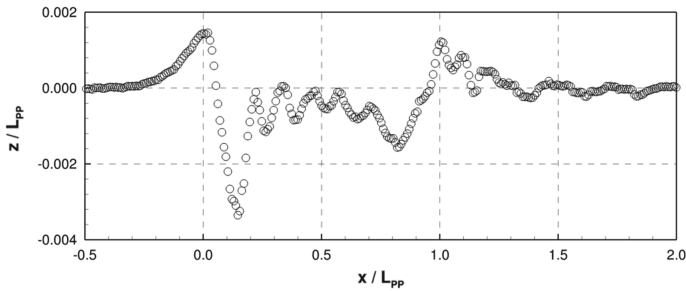
Fig. 39 Wave profile on the hull

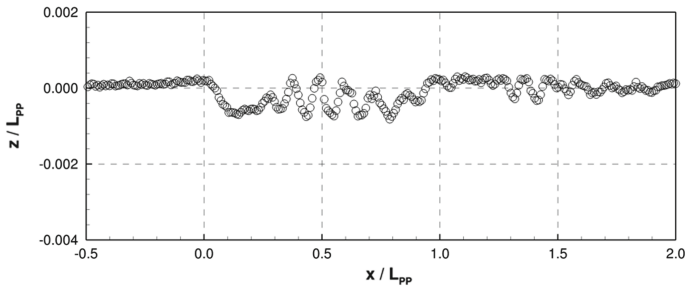**Fig. 40** Longitudinal wave cut at $y/L_{PP} = 0.1043$

Fig. 41 Longitudinal wave cut at $y/L_{PP} = 0.1900$

Resistance, sinkage, trim, self-propulsion factors with and without the duct are acquired by the tank tests at NMRI and OU. Wave field data is measured at the NMRI towing tank.

The detailed flows fields in seven stations in a stern region are measured by using SPIV in the tanks of NMRI and OU. The data are acquired in towed and self-propelled conditions without and with the duct. In addition, LDV/SPIV measurement is conducted at the TUHH wind tunnel.

For the SPIV measurement at NMRI, the error estimates are carried out using the uniform flow test results and the statistical convergence analysis of the actual measurement. It turned out that uncertainty of the velocity measurement is approximately $2-3\%$ of the uniform flow and the uncertainty of TKE measurement is approximately 1% of the square of the uniform flow magnitude. Uncertainty of v velocity is largest and this may be attributed to the problem with the reflection mirror setting.

For the mean velocity components, the data of three facilities are generally in good accordance in spite of some problems such as the laser reflection in TUHH measurement or the reflection mirror problem in NMRI measurement.

On the other hand, it is found that there is a large difference in the measured TKE levels between NMRI and OU/TUHH. Examination of the statistical convergence of NMRI measurement shows that the difference between NMRI and other facilities does not seem to come from the statistical convergence, though apparently the more frames are needed for the accurate estimation of turbulent quantities. The effect of Reynolds number difference is also investigated for the local TKE distributions along the horizontal lines at the shaft height near the propeller plane. The distributions in the bare-hull towing condition are compared in the various scaling. It appears that the TKE distributions look more wake-like rather than boundary-layer-like from the comparisons with the flat plate data. However, it is rather difficult to specify the exact reason for differences of the extremely higher TKE of NMRI data. Further investigations, such as additional measurements in different facilities and/or different measuring systems, are desirable for obtaining the reasonable distributions of TKE.

Finally, the recommendations to the future workshops at present are as follows:

For the resistance and self-propulsion, sinkage and trim and the wave profiles, the measured data from NMRI can be considered to be appropriate. For the local flow data, the OU data seems to have no serious deficiencies and thus can be recommended as the reliable measured data of mean velocities. Further works will be needed to establish reliable turbulence data of this JBC case.

References

Hino, T., Hirata, N., Ohashi, K., Toda, Y., Zhu, T., Makino, K., et al. (2016). Hull form design and flow measurements of a bulk carrier with an energy-saving device for CFD validations. In *Proc. 13th International Symposium on Practical Design of Ships and Other Floating Structures*. Denmark: Copenhagen.

Jufuku, N., Hori, M., Itou, S., Toda, Y., & Hinatsu, M. (2015). SPIV stern flow measurement around operating propeller for with and without duct condition of Japan bulk carrier (in Japanese). In *Conference Proceedings of the Japan Society of Naval Architects and Ocean Engineers* (Vol. 21, pp. $309-312$).

Shevchuk, I., Sahab, A., Stern, F., & Abdel-Maksoud, M. (2020). Experimental and numerical studies of the flow around the JBC hull form at straight ahead condition and 8° drift angle. In *Proc. the 33rd Symposium on Naval Hydrodynamics*. Japan: Osaka.

Yoon, H., Longo, J., Toda, Y., & Stern., F. (2015). Benchmark CFD validation data for surface combatant 5415 in PMM maneuvers – Part II: Phase-averaged stereoscopic PIV flow field measurements. *Ocean Engineering, 109*, 735–750.

Longo, L., Huang, H. P., & Stern, F. (1998). Solid/free-surface juncture boundary layer and wake. *Experiments in Fluids, 25*, 283 − 297.

Lee, S. -J., Kim, H. -R., Kim, W. -J., & Van, S. –H. (2003). Wind tunnel tests on flow characteristics of the KRISO 3,600 TEU containership and 300 K VLCC double-deck ship models. *Journal of Ship Research*, *47*(1), 24 − 38.